Article

Self-Isolated Dual-Mode High-Pass Birdcage RF Coil for Proton and Sodium MR Imaging at 7 T MRI

You-Jin Jeong [1], Suchit Kumar [2], Seon-Woo Park [2], Youngkyu Song [3], Jee-Hyun Cho [3], Chan Hong Moon [4] and Chang-Hyun Oh [1,2,*]

1 Department of Electronics and Information Engineering, Korea University, Sejong 30019, Republic of Korea; yuja91@korea.ac.kr
2 Research Institute for Advanced Industrial Technology, Korea University, Sejong 30019, Republic of Korea; suchitkumar@korea.ac.kr (S.K.); 1004seonu@korea.ac.kr (S.-W.P.)
3 Bio-Chemical Analysis Team, Korea Basic Science Institute, Cheongju 28119, Republic of Korea; jhcho@kbsi.re.kr (J.-H.C.)
4 Department of Radiology, University of Pittsburgh, Pittsburgh, PA 15213, USA; moonc@upmc.edu
* Correspondence: ohch@korea.ac.kr; Tel.: +82-2-3290-3984

Abstract: This study presents the feasibility of a dual-mode high-pass birdcage RF coil to acquire MR images at both ^{1}H and ^{23}Na frequencies at ultra-high-field MR scanner, 7 T. A dual-mode circuit (DMC) in the dual-mode birdcage (DMBC) RF coil operates at two frequencies, addressing the limitations of sensitivity reduction and isolation between two frequencies as in traditional dual-tuned RF coil. Finite-difference time-domain (FDTD) based electromagnetic (EM) simulations were performed to verify the RF coil at each frequency on the three-dimensional human head model. The DMBC RF coil resonated at proton (^{1}H) and sodium (^{23}Na) frequencies, and also single-tuned high-pass birdcage RF coils were constructed for both ^{1}H and ^{23}Na frequencies. The bench test performance of the RF coils was evaluated using network analysis parameters, including the measurement of scattering parameters (S-parameters) and quality factors (Q-factors). Q-factor of the DMBC coil at ^{1}H port was 10.2% lower than that of ^{1}H single-tuned birdcage (STBC) coil, with a modest SNR reduction of 6.5%. Similarly, the Q-factor for the DMBC coil at ^{23}Na port was 12.3% less than that of ^{23}Na STBC coil, and the SNR showed a minimal reduction of 5.4%. Utilizing the DMBC coil, promising ^{1}H and ^{23}Na MR images were acquired compared to those by using STBC coils. In conclusion, deploying a DMBC ^{1}H/^{23}Na coil has been demonstrated to overcome traditional constraints associated with dual-tuned RF coils, achieving this with only nominal signal attenuation across both nuclei operational frequencies.

Keywords: magnetic resonance imaging; sodium MRI; dual-mode RF coil; dual-tuned RF coil; ultra-high-field MRI; EM simulation

1. Introduction

Sodium (^{23}Na) magnetic resonance imaging (MRI) offers valuable physiological and pathological information beyond conventional proton (^{1}H) MRI with insights into intracellular and extracellular ^{23}Na concentrations, which serve as an indicator of cellular metabolism and function. Mainly, ^{23}Na MRI is beneficial for assessing tissue viability and cellular integrity in various diseases such as tumors, ischemia, brain disorders including stroke and epilepsy, and neurodegenerative diseases such as multiple sclerosis and Alzheimer's disease, etc. [1–9].

However, ^{23}Na has a lower gyromagnetic ratio (γ_{23Na} = 11.25 MHz/T, whereas γ_{1H} = 42.58 MHz/T) by a factor of approximately 3.8, and it exists in lower natural abundance in the human body compared to the ^{1}H, resulting in inherently weaker signal intensity [10–13]. This results in a lower signal-to-noise ratio (SNR) in MRI, requiring the application of stronger magnetic fields such as ultra-high-field (UHF) scanners, 7 T and

dedicated RF coils to achieve adequate image quality [14]. Additionally, the intracellular sodium ions have short relaxation times of about 0.5–5 ms, which demands the implementation of rapid acquisition techniques to capture sufficient signals, which is technically challenging. In addition, high-resolution ^{1}H anatomy imaging is required for the appropriate interpretation of measured sodium concentration from [23]Na MRI. Despite these challenges, ongoing research has focused on enhancing the feasibility and reliability of ^{1}H/[23]Na MRI by developing more sensitive coils, optimizing the pulse sequences, and employing quantitative analysis techniques [15–21].

Enhancing the quality of [23]Na MRI necessitates the optimization of RF coils specifically designed for [23]Na imaging. Several designs and schemes exist for [23]Na RF coil construction such as single-tuned RF coils, single-tuned RF coils with ^{1}H frequency blocking circuit, and dual-tuned ^{1}H/[23]Na RF coils [13,22–31]. When using the single-tuned RF coil for ^{1}H and [23]Na separately, co-registration of two images is essential; however, this approach often results in errors in [23]Na images due to poor B_0 shimming. So, [23]Na coil would be better designed to operate within ^{1}H coil to facilitate the automatic co-registration of both nuclei images. At the same time, positioning the coil loops close to the imaging object is advantageous in the increase in coil sensitivity. However, for the brain imaging with a size of 150–200 mm diameter, the spatial constraints limit the feasibility of incorporating [23]Na coil loops into outer volume ^{1}H coil, if two separate nuclei coils are designed. As an alternative design approach, dual-tuned RF coil becomes advantageous in addressing spatial limitation and also facilitating the integration of multi-channel reception capabilities for advanced imaging techniques. Various techniques have been developed to enable the dual-tuning of RF coils for acquiring proton and x-nuclei MRI at the same experimental setting. These include active switching mechanisms employing pin-diodes to modulate circuit resonance [26,27], the implementation of trap circuits along the leg of the birdcage RF coil to shift or block specific frequencies [28–30], and the incorporation of a four end-ring architecture designed to resonate simultaneously at two distinct frequencies [31,32]. The pin-diode switching technique is widely utilized due to the availability of pin-diode DC bias drivers in MR scanner, while the pin-diode activation results in a sensitivity reduction. Specifically, when the pin-diode is forward-biased, there is a significant decrease in the SNR of approximately 35% compared to a single-tuned RF coil configuration [26,33]. Meanwhile, frequency-specific blocking traps can be integrated into each leg of a single birdcage RF coil structure to achieve dual-tuning. This approach halves the number of active legs at each frequency, necessitating a doubling of the leg count to preserve the homogeneity of the B_1 field. The trap can be utilized as a frequency-shifting (FS) circuit with an additional capacitor to resonate the single birdcage RF coil at two frequencies. Employing the FS trap circuits to tune at a lower frequency results in a performance degradation of the RF coil at high frequencies. In other words, the resonance of the RF coil at a lower frequency comes at the expense of its efficiency at a higher frequency [34]. Additionally, the FS trap is not designed for any two resonant frequencies, and adjusting the trap and capacitor values for dual-tuning is complicated. Moreover, the operation of the FS traps presents a challenge when the target frequencies are in close proximity. Alternatively, a four end-ring design, usually comprising a low-pass and high-pass birdcage RF coil without lossy components, offers superior SNR compared with the alternating legs of a birdcage coil with traps [35]. However, it requires an optimized inner to outer rung length ratio, leading to an increase in the overall coil length. This increase in the RF coil length consequently restricts the accessible space for patients, presenting a challenge for applications in brain imaging. The advantages and challenges of existing dual-tuned RF coil designs are summarized in Table 1.

Table 1. Advantages and challenges of several dual-tuned RF coil design.

Design Type	Advantages	Challenges
Active switching with pin-diode [26,27,33]	Widely utilized due to available pin-diode drivers in MR systems	Sensitivity reduction when the pin-diode is forward-biased
FS trap circuit [28,29]	Achieves dual-tuning at two frequencies using a single birdcage RF coil	Performance degradation at proton frequency Complex adjustment of trap and capacitor values
Frequency blocking trap circuit [30]	Allows dual-tuning by integrating traps into each leg of a single birdcage RF coil	Requiring a doubling of leg count for B_1 field homogeneity
Four end-ring [31,32]	Superior SNR compared to alternating leg designs. No additional lossy components	Increasing overall coil length and restricting patient space, especially in brain imaging

In response to the limitations presented by existing dual-tuning methods in RF coil design, the study introduces a self-isolated dual-tuned high-pass birdcage RF coil, termed the dual-mode birdcage (DMBC) RF coil. The DMBC RF coil is physically a single birdcage RF coil of precisely the combination of two single-tuned high-pass birdcage RF coil operating at each ^{1}H and [23]Na frequency without additional end-rings and active switching components. The DMBC RF coil is simultaneously tuned to two distinctive homogeneous modes at two different frequencies. The design features a dual-mode circuit (DMC) that utilizes a trap circuit specifically for tuning at the [23]Na resonant frequency. This configuration enables tuning at the ^{1}H frequency exclusively through the end-ring capacitors, as the same approach used in single-tuned birdcage (STBC) RF coils. Thus, the DMC allows the separate control of the DMBC RF coil to be tuned effectively at two frequencies. The utility of the DMBC RF coil with DMC was verified through ^{1}H and [23]Na MRI experiments at 7 T human scanner to maximize [23]Na signal sensitivity, and the images were compared with those ^{1}H and [23]Na image acquired by STBC RF coils.

2. Materials and Methods

2.1. FDTD EM Simulation

Electromagnetic (EM) simulation based on finite difference time domain (FDTD) [36] was utilized to predict the RF coil's performance at both the ^{1}H and [23]Na frequency using Sim4Life (ZMT, Zurich MedTech AG, Zurich, Switzerland) [37]. A 12-leg high-pass tapered birdcage RF coil, as shown in Figure 1, was designed for both ^{1}H and [23]Na transmission and reception based on the following specifications: upper diameter = 153 mm; bottom diameter = 250 mm; length of legs = 210 mm; width of legs and end-rings = 20 mm; resonant frequency of [1]H = 298 MHz; resonant frequency of [23]Na = 78.9 MHz at 7 T. The optimized capacitor values were calculated through the RF circuit co-simulation method [38], which provides more reliable capacitor values compared to the previous birdcage calculator based on inductance measurement [39]. For the ^{1}H coil simulation, the end-ring capacitors were 3.7 pF and 2.6 pF for the upper and bottom end-ring, respectively. For the [23]Na coil simulation, capacitors of 85.5 pF and 45.35 pF were used at the upper and bottom end-ring. These simulations were performed on a three-dimensional (3D) human model, "Duke" [40], to assess B_1^+-field uniformity and specific absorption rate (SAR). The B_1^+-field uniformity was calculated in the human model at the center of the RF coil.
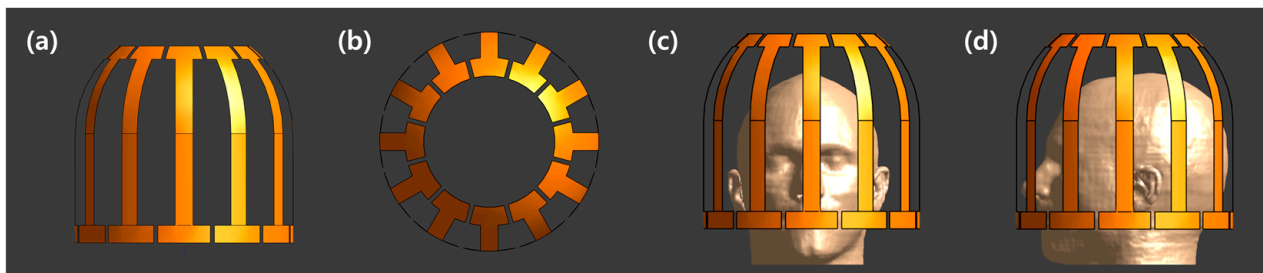
Figure 1. Simulation design for tapered birdcage RF coil for ^{1}H and ^{23}Na in (**a**) front view and (**b**) top view; Simulation set-up with the 3D human head model in (**c**) front view and (**d**) side view.

2.2. Single-Tuned Birdcage (STBC) RF Coil

A 12-leg high-pass tapered birdcage RF coil, as shown in Figure 2, was designed to enhance signal intensity at the apex of the brain for both ^{1}H and ^{23}Na resonant frequencies at 7 T. The legs and end-rings were constructed using copper sheets with a thickness of 0.15 mm and widths of 20 mm. An acrylic plastic frame was used to fabricate a support coil frame, consisting of a large cylindrical tube (250 mm outer diameter and 180 mm length), a partial hemisphere (250 mm diameter and 110 mm length), and a small cylindrical tube (115 mm outer diameter and 120 mm length) with a thickness of 5 mm. The diameters of the RF coil at the bottom and the apex of the RF coil were 250 mm and 153 mm, respectively. The length of each leg was 210 mm, and the legs were attached along the outer surface of the acrylic frame.
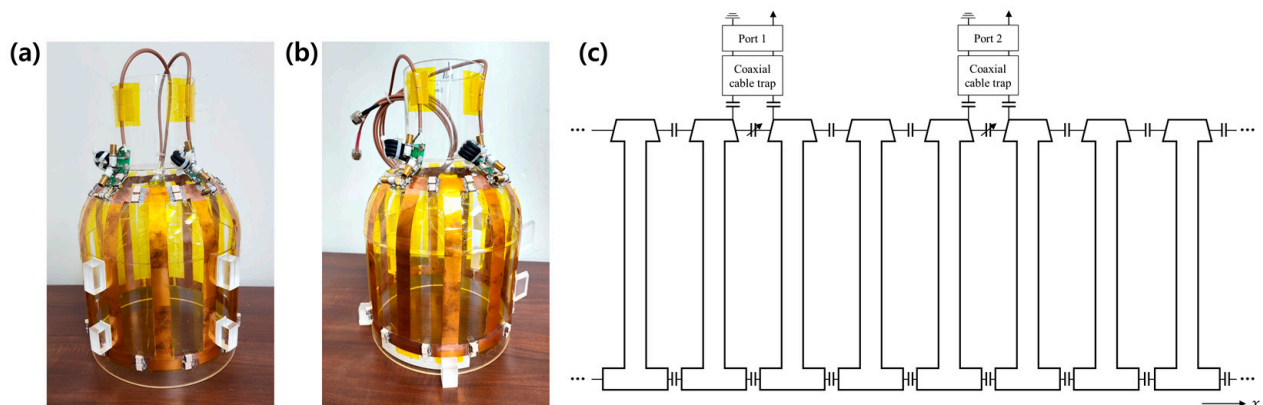

Figure 2. (**a**) Constructed ^{1}H STBC RF coil; (**b**) constructed ^{23}Na STBC RF coil; (**c**) schematic of the STBC RF coil, shown in an unfolded view; x-axis is the perimeter. Trimmer capacitors are utilized to fine-tune both ^{1}H and ^{23}Na STBC RF coils. The depicted section of the circuit includes key components; the remaining four legs are omitted.

Each ^{1}H and ^{23}Na STBC RF coil port was tuned to the homogeneous mode at 298 MHz and 78.9 MHz. High-quality factor (Q-factor) and high RF power capacitors (DLC70E, Dalicap Tech. Corporation, Dalian, China) were attached at the end-ring to tune the RF coil to the desired resonance mode and trimmer capacitors with high Q-factors (Q-factor > 3000, capacitance range = 1.0–14.0 pF, working voltage = 1250 V, non-magnetic, Voltronics, Denville, NJ, USA) were attached at the end-ring of each feeding points to fine-tune the RF coil. For the ^{1}H STBC RF coil, capacitors of 4.3 pF and 3.2 pF were connected to the upper and bottom end-ring, excluding the ports. In the case of the ^{23}Na STBC RF coil, capacitors of 102 pF and 55.2 pF were similarly attached to the upper end-ring and bottom end-ring, excluding the ports. Shielded coaxial cable traps were connected after the matching circuit to mitigate the propagation of common-mode currents along the coaxial cable shield [41]. For the bench test of both the ^{1}H and ^{23}Na STBC RF coils, the scattering (S) parameters

and Q-factors (at 3 dB bandwidth) were measured and analyzed using a vector network analyzer (N9913A, Agilent Technologies, Santa Clara, CA, USA).

2.3. ^{1}H/^{23}Na Dual-Mode Birdcage (DMBC) RF Coil [42]

The DMBC RF coil was designed with same size and structure as the STBC RF coil described in Section 2.2, including the coil frame. Meanwhile, the DMC was employed at each end-ring to tune the RF coil at ^{23}Na resonant frequency. The DMC comprises two capacitors (C_1 and C_2) and one inductor (L), as shown in Figure 3. In this configuration, the parallel LC_1 circuit operates as an open circuit, specially designed to resonate at ^{1}H resonant frequency, and its impedance goes infinity. On the other hand, the LC_1 circuit acts as an inductive circuit (L_{eq}) at the ^{23}Na resonant frequency. The series L_{eq} and C_2 work as a capacitive circuit (C_{eq}), so the addition of the equivalent capacitance facilitates the tuning of the RF coil at ^{23}Na frequency. Thus, the DMC functions as additional capacitance for tuning at ^{23}Na resonant frequency without affecting the end-ring capacitor (C_H) for tuning the ^{1}H resonant frequency [42]. In other words, the combined capacitance of the C_{eq} and C_H functions equivalently to the end-ring capacitor in the ^{23}Na STBC RF coil. The impedance of the DMC at ^{1}H and ^{23}Na resonant frequency (Z_H and Z_{Na}) and the C_{eq} of the DMC at ^{23}Na resonant frequency can be described as follows:

$$Z_H(\omega) = \frac{1}{\frac{1}{j\omega_H L} + j\omega_H C_1} + \frac{1}{j\omega_H C_2} \tag{1}$$

$$Z_{Na}(\omega) = j\omega_{Na}L_{eq} + \frac{1}{j\omega_{Na}C_2} \\ = \frac{1}{j\omega_{Na}C_{eq}} \tag{2}$$

$$\omega_H = \frac{1}{\sqrt{LC_1}} \tag{3}$$

$$C_{eq} = \frac{C_2}{1 - \omega_{Na}^2 C_2 L_{eq}} \tag{4}$$

where ω_H and ω_{Na} are the resonant frequency of ^{1}H and ^{23}Na at 7 T, respectively. The impedance and capacitance of the DMC along 1 to 400 MHz were calculated with the following values of each component: L = 95 nH; C_1 = 3 pF; C_2 = 28.24 pF; C_H = 4.3 pF. The capacitance of the C_H is chosen for the same value with the upper end-ring capacitor of the ^{1}H STBC RF coil, and L and C_1 are chosen to the practical values of the DMC in the DMBC RF coil. The capacitance of the C_2 was selected to operate the combination of DMC and C_H as the capacitance of 102 pF at ω_{Na} which was used for upper end-ring capacitor of the ^{23}Na STBC RF coil. Calculated impedances of the DMC at ω_{Na} and ω_H were $-j20.62$ Ω and $-j5.8$ MΩ, respectively. Capacitances computed from the impedance of the DMC at ω_{Na} and ω_H were 97.7 pF and 0.00009 pF, respectively. At the ω_H, the impedance of the DMC is extremely high, and the capacitance is small enough to reject the current, so the DMC operates as close to open state. To compare with the FS trap based dual-tuning method [28,29], the impedance of the FS trap was calculated along the frequency range of 1 to 400 MHz. The circuit with FS trap comprises the same components as DMC (L_T: inductor of FS trap, C_{T_1}: capacitor of FS trap, C_{T_2}: additional capacitor for dual-tuning), but not resonate at the ^{1}H frequency. In this case, there are infinite combinations of component values available. Therefore, to ensure that the FS trap does not resonate at 298 MHz, we selected the same inductance value for the L_T as used in the DMC and an arbitrary C_{T_1} of 8.2 pF. The C_{T_2} of 25.8 pF was chosen to operate the circuit as the capacitance of 102 pF and 4.3 pF at ω_{Na} and ω_H, respectively. Impedances of the combination of DMC with end-ring capacitor C_H and FS trap with C_{T_2} at ω_{Na} and ω_H were $-j19.75$ Ω and $-j124.2$ Ω, respectively. The FS trap-based circuit allows for the creation of two different capacitances. However, adjusting the component values during the practical construction of the RF coil proves complex. This complexity arises because the FS trap is designed not to resonate at any frequencies other than those designated for ω_{Na} and ω_H, as previously mentioned.

All circuit analyses were conducted under the ideal condition, with the assumption of negligible resistance of the inductance or capacitance.
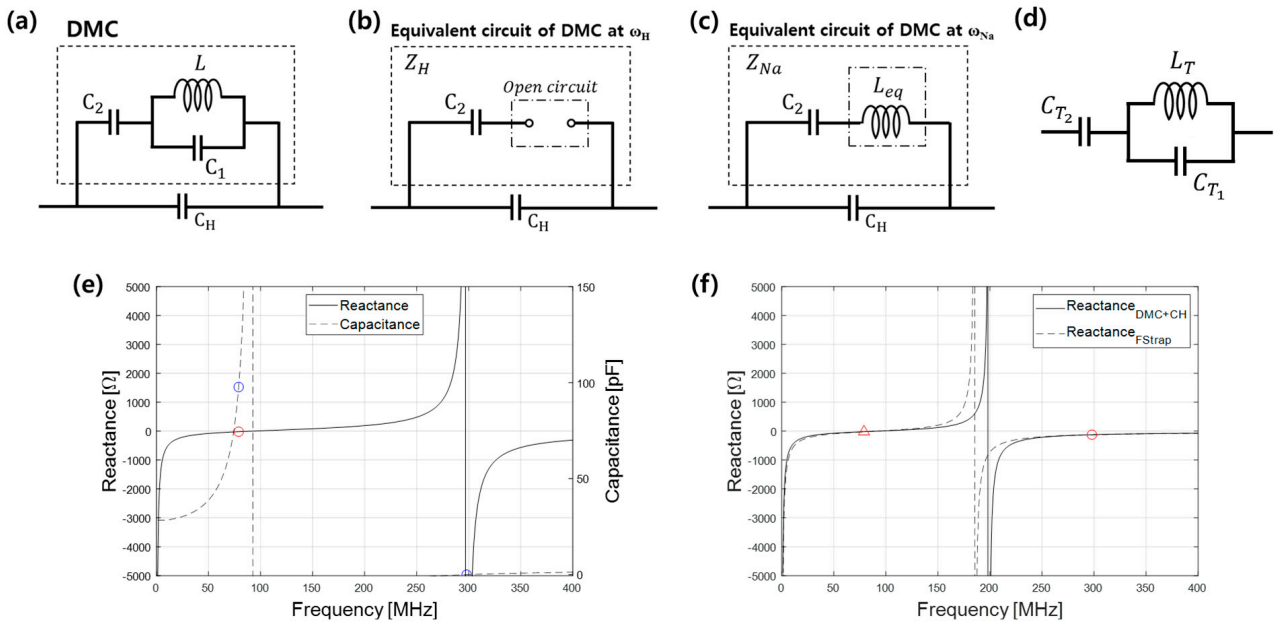

Figure 3. (**a**) Circuit diagram including DMC and C_H; the equivalent circuit of the DMC comprises an equivalent form of the parallel LC_1 circuit and C_2 (**b**) at ω_H and (**c**) ω_{Na}; (**d**) circuit diagram of the FS trap based dual-tuning circuit; (**e**) calculated reactances (imaginary part of the impedance) and capacitances of the DMC with ideal values along the frequency range of 1–400 MHz. Reactances at ω_{Na} (red circle) and ω_H are $-20.62\ \Omega$ and $-5.8\ \text{M}\Omega$ (almost infinity), respectively. Capacitances at ω_{Na} and ω_H depicted with blue circles are 97.7 pF and 0.00009 pF, respectively; (**f**) calculated reactances of the combination of DMC and C_H, and the FS trap along the frequency range of 1–400 MHz. The reactance at ω_{Na} pointed by the red triangle is $-19.75\ \Omega$. Also, the reactance at ω_H pointed by the red circle is $-124.2\ \Omega$.

A dual-frequency trap was designed for both ω_H and ω_{Na}, comprising RG-58 cable and two capacitors. As shown in Figure 4, two capacitors (C_{trap_H} and $C_{trap_{Na}}$) are connected in parallel to the inductor (L_{trap}) with mutual inductance being used for both capacitors to enable operation at two frequencies.
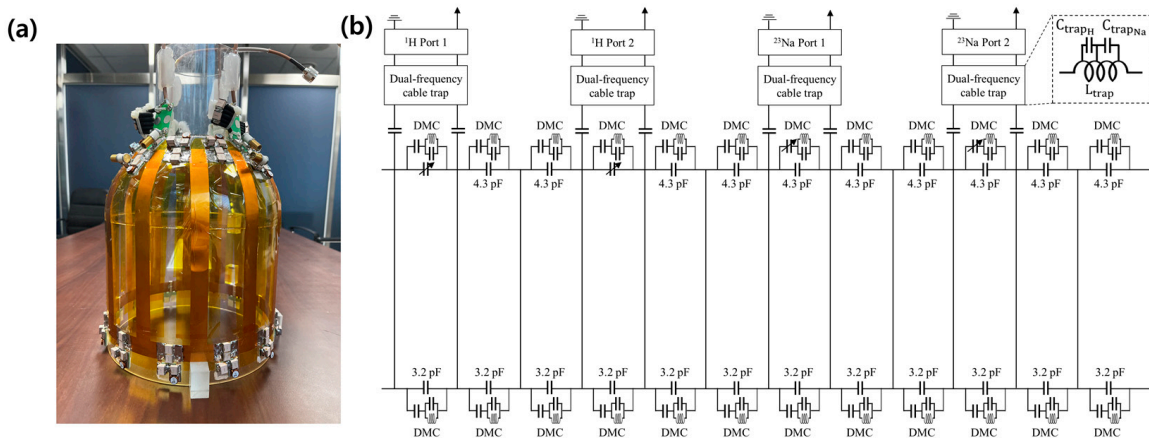

Figure 4. (**a**) Constructed DMBC RF coil; (**b**) comprehensive circuit diagram of DMBC RF coil, including the DMC and dual-frequency cable trap design.

Each port of the ^{1}H/^{23}Na DMBC RF coil was individually tuned to the homogeneous mode at ω_{Na} and ω_H. At the end-ring, capacitors of 4.3 pF and 3.2 pF were connected to the upper end-ring and bottom end-ring, respectively, the same as the ^{1}H STBC RF coil to tune at 298 MHz. The equivalent capacitance of the DMC was added to each end-ring for tuning at 78.9 MHz. The DMC was constructed with the following components' values: L = 95 nH; C_1 = 3 pF; C_2 for upper DMC = 30.6 pF; C_2 for bottom DMC = 24.2 pF. Capacitances of the upper and bottom DMC at ω_{Na} were 97.8 pF and 51.8 pF, respectively. At ω_H, the DMC functioned as an open circuit, with the capacitance of less than 0.001 pF, which was sufficiently small to be considered immeasurable. Trimmer capacitors were attached at the end-ring of ^{1}H ports and C_2 of DMC of ^{23}Na ports to fine-tune the RF coil. Bench tests at the ^{1}H and ^{23}Na frequency were performed as described in Section 2.2.

2.4. MR Imaging Experiment

The imaging performances of STBC RF coils and DMBC RF coil were tested in a human 7 T scanner (Achieva 7.0 T, Philips, Amsterdam, The Netherlands) at the Korea Basic Science Institute in Cheongju, Republic of Korea. To ensure the stable positioning of the RF coils on the patient table, we utilized an additional cylindrical frame assembly (with an outer diameter of 370 mm and an inner diameter of 300 mm). Additionally, the RF coil frame supporters were employed to secure the RF coil frame, preventing any movement during the experiments. After the RF coil frame was securely positioned, a head support was placed between the participant's head and the RF coil frame, and additional foam pads were employed to stabilize the head, preventing movement during the MR imaging. For both the ^{1}H and ^{23}Na MR experiment, we employed the scanner vendor's ^{1}H-^{23}Na Transmit/Receive (T/R) interface box. This approach ensured that all experiments were conducted under consistent conditions, particularly regarding the RF power limitations specific to each nuclei's STBC and DMBC RF coils. The STBC RF coils were tested for both ^{1}H and ^{23}Na MRI. For the ^{1}H MR experiments, B_1^+-field mapping was performed on a cylindrical phantom (inner diameter of 160 mm; length of 200 mm) using an actual flip-angle imaging (AFI) method [43], and T1-weighted magnetization-prepared rapid gradient-echo (MPRAGE) imaging was performed on the human brain [44], to investigate B_1 inhomogeneity at large flip-angle (FA). For the ^{23}Na experiments, the B_1^+-field mapping was performed on the cylindrical phantom using the double-flip angle method (DAM) [45], and ^{23}Na images were obtained using an ultra-short echo-time (UTE) sequence on the human brain [17,20]. Because of the low signal intensity of ^{23}Na in the brain, the B_1^+-field mapping was conducted on a high sodium concentration phantom, consisting of a 1 g/L of copper sulfate and 154 mM of sodium chloride solution. A two-dimensional (2D) stacked radial projection sequence was employed for all ^{23}Na imaging to reduce the echo-time (TE), and the number of projections was 3000 for phantom imaging and 6000 for in vivo head imaging. All experiments were performed in strict compliance with established safety guidelines for experimental RF hardware in MRI [46,47], ensuring that the SAR remained within the prescribed limits of the MRI system. The human study was approved by the institutional review board of Korea University, and written informed consent was obtained from the volunteers before the experiment commenced. The detailed sequence parameters are shown in Table 2.

Table 2. MR sequence parameters for ^{1}H and ^{23}Na MRI.

	^{1}**H MRI**		^{23}**Na MRI**	
Sequence	Dual-TR (AFI)	T$_1$-weighted MPRAGE	UTE (DAM)	UTE
Nominal FA (°)	60	7	45 and 90	32
TE/TR (ms)	3.9/20 and 120	2.6/5.5	0.19/120	0.19/100

Table 2. *Cont.*

	¹H MRI		²³Na MRI	
FOV (mm^3)	$240 \times 240 \times 240$	$240 \times 240 \times 240$	$240 \times 240 \times 240$	$240 \times 240 \times 240$
Acquisition matrix	120×120	240×240	-	-
Reconstruction matrix	120×120	240×240	68×68	68×68
Image resolution (mm^2)	2×2	1×1	3.5×3.5	3.5×3.5
Slice thickness (mm)	8	1	8	8
Average	1	1	1	3
Scan time (min)	2 min 47 s	6 min 6 s	6 min 1 s	30 min

SNR maps were calculated in in vivo MR images, as follows:

$$\text{SNR} = \frac{\text{Signal Intensity}}{\text{Average standard deviation of ROI}_s} \tag{5}$$

where the average standard deviation of the region-of-interest (ROI) represents the average standard deviation of the noise in four ROIs of noise-only background region outside the brain. The uniformity of FA was calculated in 2D ROI within the MR images as follows [48]:

$$\text{Uniformity}(\%) = \left[1 - \frac{I_{\max} - I_{\min}}{I_{\max} + I_{\min}} \right] \times 100 \tag{6}$$

where $I_{\max}$ and $I_{\min}$ represent the maximum and minimum values in FA maps, respectively. FA and SNR maps were calculated and reconstructed using MATLAB (R2022b, MathWorks Inc., Natick, MA, USA).

3. Results

3.1. EM Simulation

Figure 5 shows the B_1^+-field and SAR maps normalized to 1 μT of the total input power for the tapered high-pass birdcage RF coil at its resonant frequency for ¹H and ²³Na. The B_1^+-field uniformity measured at the central axial plane of the RF coil was quantified to be 64.5% at the ¹H frequency. In contrast, at the ²³Na resonant frequency, the field uniformity was 90.2%.

3.2. Bench Test Measurements

The bench test results for the ¹H and ²³Na STBC, and DMBC RF coils at both ¹H and ²³Na ports are listed in Table 3. During the measurement of the S-parameter and Q-factor for each port of the DMBC RF coil, ports corresponding to the alternate frequency were terminated with a 50-ohm impedance to ensure isolation and accurate parameter assessment. An in vivo human brain was loaded inside STBC RF coils and DMBC RF coils for all measurements.

Table 3. S-parameters and Q-factor measurement for ¹H, ²³Na STBC RF coil, and ¹H/²³Na DMBC RF coil in loaded conditions. All the parameters were measured with loading of the human head.

	¹H RF Coil		²³Na RF Coil	
	STBC Coil	**DMBC Coil**	**STBC Coil**	**DMBC Coil**
Reflection Coef. (S11)	−37.98 dB	−33.62 dB	−41.85 dB	−37.95 dB
Reflection Coef. (S11)	−38.23 dB	−33.97 dB	−40.11 dB	−37.24 dB

Table 3. *Cont.*

	¹H RF Coil		²³Na RF Coil	
	STBC Coil	**DMBC Coil**	**STBC Coil**	**DMBC Coil**
Isolation Coef. (S12)	−19.10 dB	−19.23 dB	−20.71 dB	−20.31 dB
Impedance (Z11)	$50 - j\,2.33$	$50 - j\,2.52$	$50 - j\,1.81$	$50 + j\,1.14$
Impedance (Z22)	$50 - j\,1.25$	$50 - j\,3.34$	$50 - j\,0.79$	$50 - j\,1.27$
Q-factor	820.01	736.37	981.52	860.34
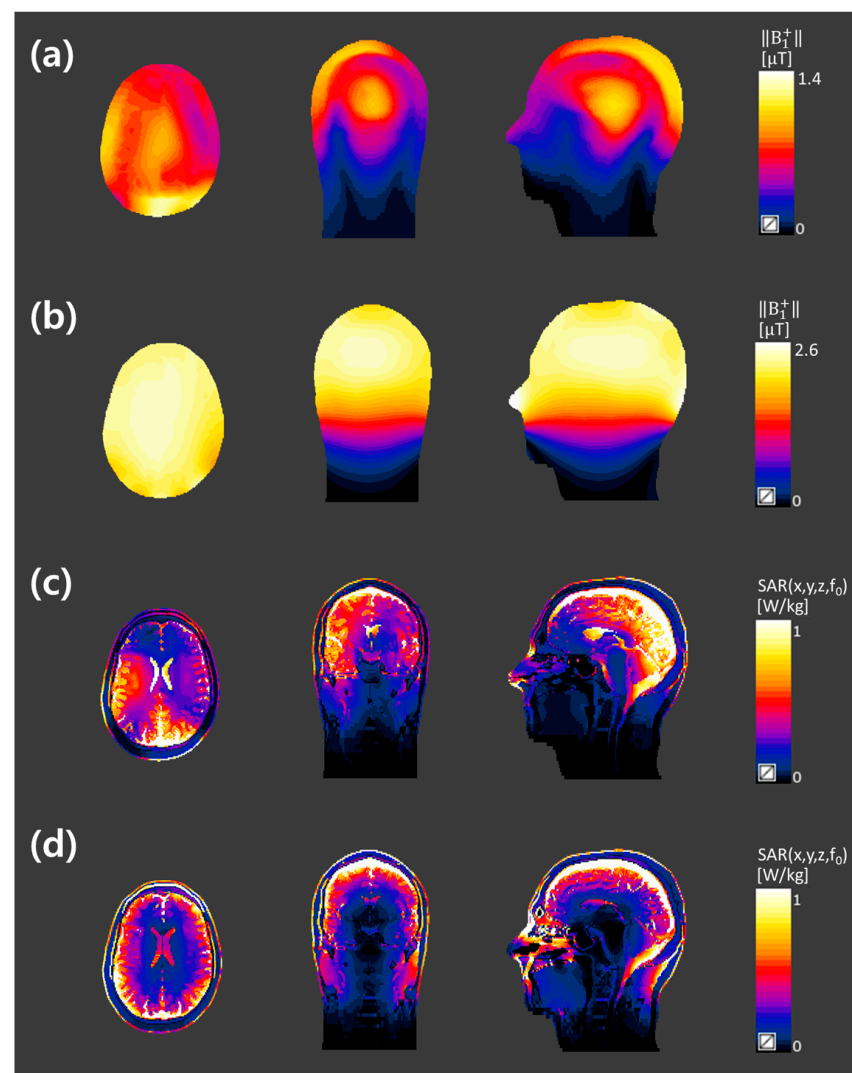
Figure 5. Simulated B_1^+-field maps in 3D human Duke model (left-axial; center-coronal; right-sagittal) at (**a**) ^{1}H and (**b**) ^{23}Na resonant frequency; simulated SAR maps in Duke model (left-axial; center-coronal; right-sagittal) at (**c**) ^{1}H and (**d**) ^{23}Na resonant frequency.

3.3. MR Imaging Experiments

Figure 6 illustrates an FA map of the phantom acquired using ^{1}H STBC RF coil, ^{23}Na STBC RF coil, and ^{1}H/^{23}Na DMBC RF coil. For the ^{1}H images, the FA map uniformity of 63.4% with ^{1}H STBC RF coil and 59.8% with ^{1}H/^{23}Na DMBC RF coil were achieved. Similarly, for ^{23}Na FA mapping, the uniformity was high at 87.8% for ^{23}Na STBC RF coil, with ^{1}H/^{23}Na DMBC RF coil achieving a nearly equivalent uniformity of 84.4%.

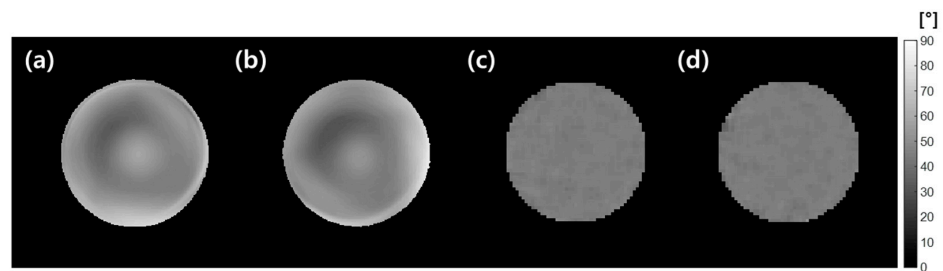**Figure 6.** ^{1}H FA map (nominal FA: 60°) of phantom obtained using (**a**) ^{1}H STBC RF coil and (**b**) ^{1}H/^{23}Na DMBC RF coil. ^{23}Na FA map (nominal FA: 45°) obtained using (**c**) ^{23}Na STBC RF coil and (**d**) ^{1}H/^{23}Na DMBC RF coil.

In the assessment of the RF coil performance for ^{1}H MRI, SNR maps using ^{1}H STBC and ^{1}H/^{23}Na DMBC RF coils are presented in Figure 7. The mean SNR value in ROI was 83.3 for ^{1}H STBC RF coil and 77.9 for ^{1}H/^{23}Na DMBC RF coil, indicating a 6.5% SNR reduction with the DMBC RF coil.
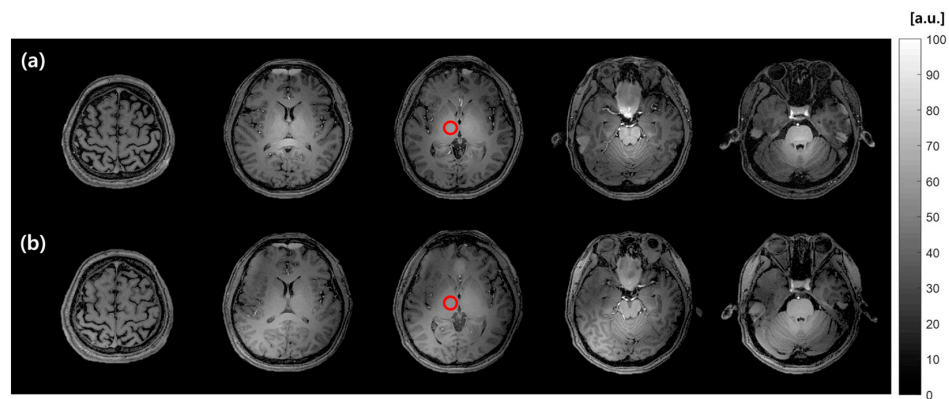
Figure 7. SNR maps of in vivo human head ^{1}H MR images acquired with (**a**) ^{1}H STBC RF coil and (**b**) ^{1}H/^{23}Na DMBC RF coil. Red circles indicate the ROI for the SNR measurement.

Similarly, for the ^{23}Na MRI test, the SNR maps of a human head are presented in Figure 8. The maps compare MR images acquired using ^{23}Na STBC and ^{1}H/^{23}Na DMBC RF coil. The mean SNR values within the cerebrospinal fluid (CSF) ROI were 41.9 vs. 39.8 for STBC ^{23}Na and ^{1}H/^{23}Na DMBC RF coil, respectively. This minor difference represents a nominal 5.4% reduction in SNR with the ^{1}H/^{23}Na DMBC RF coil, which is nearly comparable to the performance of the ^{23}Na STBC RF coil.
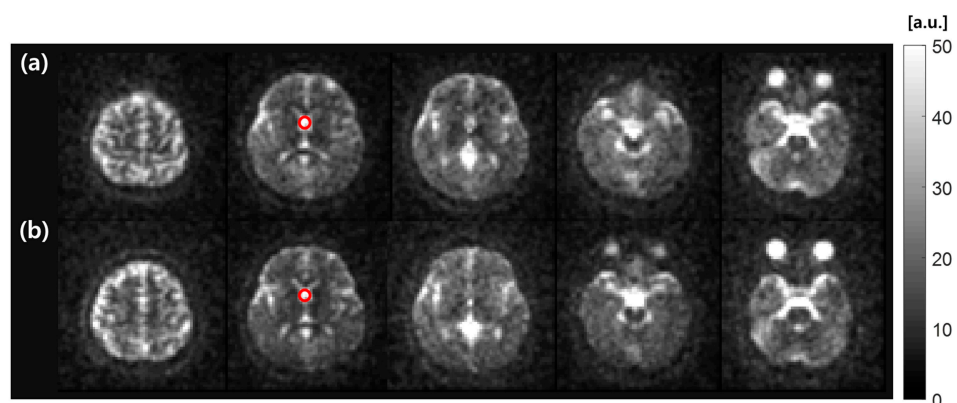

Figure 8. SNR maps of ^{23}Na MR images of an in vivo human head using (**a**) ^{23}Na STBC RF coil and (**b**) ^{1}H/^{23}Na DMBC RF coil. Red circles overlaid on CSF designate the area for SNR measurement.

4. Discussion

This study aimed to develop a novel dual-tuned birdcage RF coil capable of operation at both ^{1}H and [23]Na frequency at 7 T scanner. To achieve the goal, we proposed DMBC RF coil employing DMC, which functions as an open or capacitive circuit at two distinct frequencies. The conventional FS trap based dual-tuning method [28,29] can resonate the RF coil at two frequencies, but it is complicated to adjust the values of the components to make the desired equivalent capacitance, resulting in the signal loss at ^{1}H resonant frequency due to the existing FS trap in practical scenarios. In contrast to the FS trap based dual-tuned birdcage RF coil, the proposed DMC is designed to have minimal impact at the ^{1}H frequency, allowing the use of only end-ring capacitors, while it operates as an additional capacitance for tuning at a [23]Na frequency. While the proposed method necessitates one additional capacitor compared to FS trap-based method, it represents an optimal and intuitive strategy for achieving independent and isolated operation of the RF coil at two distinct frequencies. This design minimizes the performance degradation of DMBC RF coils compared to STBC RF coils. Thus, DMC empowers completely self-isolated and separate control for tuning at two distinct frequencies of DMBC RF coil. Either dual-mode tuning at any two frequencies, even with relatively small differences, is possible by employing DMC. In this study, we innovated a single birdcage coil design using four ports to enable quadrature driving at two different frequencies, thus realizing the dual-mode RF coil with enhanced functionality.

EM simulations were specifically conducted for the single-tuned RF coil configuration. This approach was adopted due to the operational characteristics of the DMC. At the frequency corresponding to ^{1}H resonance, the DMC effectively acts as an open circuit, rendering its influence negligible. Conversely, at [23]Na resonance frequency, the DMC functions as a capacitive circuit, essentially contributing additional capacitance to the end-ring capacitors. Consequently, the simulation did not encompass the practical effects of the DMC in real-world scenarios, as its impact is considered minimal. Therefore, to empirically validate the performance of the DMBC RF coil, STBC RF coils specific to ^{1}H and [23]Na frequencies were constructed and tested.

Bench test measurements revealed that Q-factor of DMBC RF of ^{1}H port was only 10.2% lower than that of ^{1}H STBC RF coil, with a relatively modest SNR reduction of 6.5%. Similarly, the Q-factor for DMBC RF coil for [23]Na port was 12.3% less than that of [23]Na STBC RF coil, yet the SNR showed a minimal reduction of 5.4%. The modest SNR reduction associated with DMBC RF coil can be attributed to the intrinsic trade-off characteristic of the dual-mode operation implemented by the DMC. This design element may influence the sensitivity and uniformity of the magnetic field distribution. A slight drawback of the DMBC RF coil is that when all the ports for ^{1}H and [23]Na are connected to the MRI system's interface box during the experiment, there is a potential for interference due to the influence of the alternate frequency. To address this, an additional LC filter circuit, functioning as an open circuit at the alternate frequency, could be employed to potentially enhance overall coil performance and mitigate performance degradation. Despite these considerations, the DMBC RF coil demonstrates robust performance, particularly notable for its capacity to efficiently accommodate dual-nuclei imaging applications, emphasizing its versatility and potential utility in advancing MRI technology. Moreover, the specific absorption rate (SAR) from the RF coil adheres to the safety thresholds as defined by the International Electrotechnical Commission (IEC) standards [49], ensuring the coil's safe application in clinical settings.

The acquisition time for [23]Na imaging of the human brain was considerably extended. In the study, the SAR constraint and RF power limitation inherent to the scanner prevented the application of short RF pulse duration. Consequently, the acquisition was performed with three times to enhance SNR for the measurement. Optimizing system parameters to enable short RF pulse durations, for example, <1 ms could increase [23]Na SNR, reducing the total acquisition time for human application.

Although ^{1}H and ^{23}Na images were compared, along with various coil parameter measurements for performance evaluation, between the proposed DMBC RF coil and the STBC RF coils, the study was limited to a few cases to demonstrate the feasibility of the human brain MRI. The results showed comparable imaging performance, but more population data will be needed to obtain statistical significance in future study. Particularly for ^{23}Na imaging, which inherently suffers from low signal sensitivity, achieving high resolution images presents a challenge. To address this issue, we reconstructed ^{23}Na images at a lower resolution compared to the ^{1}H images, thereby maintaining the accuracy of the results while enhancing the SNR. Moreover, further optimization of ^{23}Na imaging is required. This includes not only achieving a higher pixel resolution (below 3 mm isotropic, currently $3.5 \times 3.5 \times 8$ mm^3), but also aspects like reproducibility, and quantification of sodium concentration [20]. Additionally, the application of multi-channel reception RF coils for ^{23}Na imaging could potentially reduce acquisition time and simultaneously increase SNR, which would significantly improve both the efficiency and quality of ^{23}Na MRI.

In the study, the new coil was designed primarily for the brain study considering the potential future application to brain tumors, ischemia, brain disorders including stroke and epilepsy, and neurodegenerative diseases such as multiple sclerosis and Alzheimer's disease, etc. For achieving high quality proton and sodium imaging, such as high resolution and high signal intensity, a compact and highly sensitive coil design tailored to the human head is essential. Consequently, we proposed a single coil system capable of operating in a dual-mode, accommodating both frequencies effectively. This DMBC RF coil's benefits are not limited to brain imaging; they extend to other body parts, such as extremity imaging. With its high sensitivity, the proposed DMBC RF coil enables true simultaneous proton and sodium MR imaging, provided the scanner's receiver supports simultaneous broadband acquisition. Current state-of-the-art commercial scanners facilitate interleaved acquisition of signals at two different frequencies, allowing for alternative acquisition of signals from two nuclei [50]. Particularly, (semi-) simultaneous MRI of proton and sodium nuclei is useful in auto-coregistered abdominal imaging (in space and physiology) where the target organs exhibit non-rigid body motion. Thus, using the proposed dual-mode RF coil design for high sensitivity and simultaneous two-nuclei acquisition, whole-body MRI, including body imaging at clinical field strength like 3 T, becomes a viable option [51].

Although direct comparison of DMBC RF coil performance to dual-tuned RF coil was not performed in the study, it is speculated that DMBC RF coil, notably devoid of switching components such as pin-diodes, could eliminate performance degradation commonly associated with DC biasing in these elements. This exclusion contributes to consistent performance as it eliminates the diode-related signal losses and potential reliability issues over time, critical considerations in high-use clinical settings. Furthermore, the coil's construction with only two end-rings simplifies the overall birdcage configuration, eliminating the common patient positioning challenges encountered with more complex four end-ring dual-tuned RF coils. This streamlined design inherently allows for easier and more accurate patient positioning at the coil's center, an essential factor for achieving optimal imaging results.

5. Conclusions

In conclusion, the study has detailed the development and construction of the self-isolated DMBC RF coil designed for ^{1}H and ^{23}Na MR imaging at UHF, 7 T. Through comparative performance evaluations against STBC RF coils, we have established the utility and practicality of the DMBC RF coil, demonstrating its capacity to enhance ^{1}H and ^{23}Na MR imaging with minimal impact on image quality. Furthermore, the DMBC RF coil is not subject to the performance degradation typically caused by active switching schemes or limiting patient access, thereby offering a more efficient workflow for multi-nuclei MR imaging. The design of the DMBC RF coil is inherently flexible and can be adapted to resonate at various frequencies, accommodating a broad spectrum of x-nuclei, including ^{13}C, ^{31}P, and ^{19}F.

References

1. Ouwerkerk, R.; Jacobs, M.A.; Macura, K.J.; Wolff, A.C.; Stearns, V.; Mezban, S.D.; Khouri, N.F.; Bluemke, D.A.; Bottomley, P.A. Elevated tissue sodium concentration in malignant breast lesions detected with non-invasive ^{23}Na MRI. *Breast Cancer Res. Treat.* **2007**, *106*, 151–160. [CrossRef] [PubMed]

2. Poku, L.O.; Phil, M.; Cheng, Y.; Wang, K.; Sun, X. ^{23}Na-MRI as a Noninvasive Biomarker for Cancer Diagnosis and Prognosis. *J. Magn. Reson. Imaging* **2021**, *53*, 995–1014. [CrossRef] [PubMed]

3. Hussain, M.S.; Stobbe, R.W.; Bhagat, Y.A.; Emery, D.; Butcher, K.S.; Manawadu, D.; Rizvi, N.; Maheshwari, P.; Scozzafava, J.; Shuaib, A.; et al. Sodium imaging intensity increases with time after human ischemic stroke. *Ann. Neurol.* **2009**, *66*, 55–62. [CrossRef] [PubMed]

4. Boada, F.E.; Qian, Y.; Nemoto, E.; Jovin, T.; Jungreis, C.; Jones, S.C.; Weimer, J.; Lee, V. Sodium MRI and the Assessment of Irreversible Tissue Damage during Hyper-Acute Stroke. *Transl. Stroke Res.* **2012**, *3*, 236–245. [CrossRef] [PubMed]

5. Adlung, A.; Licht, C.; Reichert, S.; Özdemir, S.; Mohamed, S.A.; Samartzi, M.; Fatar, M.; Gass, A.; Prost, E.N.; Schad, L.R. Quantification of tissue sodium concentration in the ischemic stroke: A comparison between external and internal references for ^{23}Na MRI. *J. Neurosci. Methods* **2022**, *382*, 109721. [CrossRef] [PubMed]

6. Azilinon, M.; Makhalova, J.; Zaaraoui, W.; Medina Villalon, S.; Viout, P.; Roussel, T.; El Mendili, M.M.; Ridley, B.; Ranjeva, J.P.; Bartolomei, F. Combining sodium MRI, proton MR spectroscopic imaging, and intracerebral EEG in epilepsy. *Hum. Brain Mapp.* **2023**, *44*, 825–840. [CrossRef] [PubMed]

7. Petracca, M.; Fleysher, L.; Oesingmann, N.; Inglese, M. Sodium MRI of multiple sclerosis. *NMR Biomed.* **2016**, *29*, 153–161. [CrossRef]

8. Weber, C.E.; Nagel, K.; Ebert, A.; Roßmanith, C.; Paschke, N.; Adlung, A.; Platten, M.; Schad, L.R.; Gass, A.; Eisele, P. Diffusely appearing white matter in multiple sclerosis: Insights from sodium (^{23}Na) MRI. *Mult. Scler. Relat. Disord.* **2021**, *49*, 102752. [CrossRef]

9. Mohamed, S.A.; Herrmann, K.; Adlung, A.; Paschke, N.; Hausner, L.; Frölich, L.; Schad, L.; Groden, C.; Kerl, H.U. Evaluation of Sodium (^{23}Na) MR-imaging as a Biomarker and Predictor for Neurodegenerative Changes in Patients with Alzheimer's Disease. *In Vivo* **2021**, *35*, 429–435. [CrossRef]

10. Riemer, F.; McHugh, D.; Zaccagna, F.; Lewis, D.; McLean, M.A.; Graves, M.J.; Gilbert, F.J.; Parker, G.J.; Gallagher, F.A. Measuring tissue sodium concentration: Cross-vendor repeatability and reproducibility of ^{23}Na-MRI across two sites. *J. Magn. Reson. Imaging* **2019**, *50*, 1278–1284. [CrossRef]

11. Meyer, M.M.; Haneder, S.; Konstandin, S.; Budjan, J.; Morelli, J.N.; Schad, L.R.; Kerl, H.U.; Schoenberg, S.O.; Kabbasch, C. Repeatability and reproducibility of cerebral ^{23}Na imaging in healthy subjects. *BMC Med. Imaging* **2019**, *19*, 26. [CrossRef] [PubMed]

12. Gast, L.V.; Platt, T.; Nagel, A.M.; Gerhalter, T. Recent technical developments and clinical research-applications of sodium (^{23}Na) MRI. *Prog. Nucl. Magn. Reson. Spectrosc.* **2023**, *138–139*, 1–51. [CrossRef] [PubMed]

13. Anisimov, N.; Sadykhov, E.; Pavlova, O.; Fomina, D.; Tarasova, A.; Pirogov, Y.A. Whole body sodium MRI at 0.5 Tesla using surface coil and long echo time sequence. *Appl. Magn. Reson.* **2019**, *50*, 1149–1161. [CrossRef]

14. Niesporek, S.C.; Nagel, A.M.; Platt, T. Multinuclear MRI at ultrahigh fields. *Top. Magn. Reson. Imaging* **2019**, *28*, 173–188. [CrossRef] [PubMed]

15. Wilferth, T.; Mennecke, A.; Gast, L. Quantitative 7 Tesla ^{23}Na MRI of the human brain using a 32–channel phased-array head coil: Application to patients with secondary progressive multiple sclerosis. *NMR Biomed.* **2022**, *35*, e4806. [CrossRef] [PubMed]

16. Brown, R.; Madelin, G.; Lattanzi, R.; Chang, G.; Regatte, R.R.; Sodickson, D.K.; Wiggins, G.C. Design of a nested eight-channel sodium and four-channel proton coil for 7T knee imaging. *Magn. Reson. Med.* **2013**, *70*, 259–268. [CrossRef]

17. Dai, J.; Gosselink, M.; van der Velden, T.A.; Meliadò, E.F.; Raaijmakers, A.J.E.; Klomp, D.W.J. An RF coil design to enable quintuple nuclear whole-brain MRI. *Magn. Reson. Med.* **2023**, *89*, 2131–2141. [CrossRef] [PubMed]

18. Coste, A.; Boumezbeur, F.; Vignaud, A.; Madelin, G.; Reetz, K.; Le Bihan, D.; Rabrait-Lerman, C.; Romanzetti, S. Tissue sodium concentration and sodium T_1 mapping of the human brain at 3 T using a Variable Flip Angle method. *Magn. Reson. Imaging* **2019**, *58*, 116–124. [CrossRef]

19. Kratzer, F.J.; Flassbeck, S.; Schmitter, S.; Wilferth, T.; Magill, A.W.; Knowles, B.R.; Platt, T.; Bachert, P.; Ladd, M.E.; Nagel, A.M. 3D sodium (^{23}Na) magnetic resonance fingerprinting for time-efficient relaxometric mapping. *Magn. Reson. Med.* **2021**, *86*, 2412–2425. [CrossRef]

20. Qian, Y.; Zhao, T.; Zheng, H.; Weimer, J.; Boada, F.E. High-resolution sodium imaging of human brain at 7 T. *Magn. Reson. Med.* **2012**, *68*, 227–233. [CrossRef]

21. Zaric, O.; Beiglböck, H.; Janacova, V.; Szomolanyi, P.; Wolf, P.; Krebs, M.; Trattnig, S.; Krššák, M.; Juras, V. Repeatability assessment of sodium (^{23}Na) MRI at 7.0 T in healthy human calf muscle and preliminary results on tissue sodium concentrations in subjects with Addison's disease. *BMC Musculoskelet. Disord.* **2022**, *23*, 925. [CrossRef] [PubMed]

22. Giovannetti, G.; Pingitore, A.; Positano, V.; De Marchi, D.; Valvano, G.; Gibiino, F.; Aquaro, G.D.; Lombardi, M.; Landini, L.; Santarelli, M.F. Improving sodium Magnetic Resonance in humans by design of a dedicated ^{23}Na surface coil. *Measurement* **2014**, *50*, 285–292. [CrossRef]

23. Maril, N.; Rosen, Y.; Reynolds, G.H.; Ivanishev, A.; Ngo, L.; Lenkinski, R.E. Sodium MRI of the Human Kidney at 3 Tesla. *Magn. Reson. Med.* **2006**, *56*, 1229–1234. [CrossRef] [PubMed]

24. Yoon, J.-S.; Kim, J.-M.; Chung, H.-J.; Jeong, Y.-J.; Jeong, G.-W.; Park, I.; Kim, G.-W.; Oh, C.-H. Development of a proton-frequency-transparent birdcage radiofrequency coil for in vivo ^{13}C MRS/MRSI study in a 3.0 T MRI system. *Appl. Sci.* **2021**, *11*, 11445. [CrossRef]

25. Giovannetti, G.; Valvano, G.; Virgili, G.; Giannoni, M.; Flori, A.; Frijia, F.; De Marchi, D.; Hartwig, V.; Landini, L.; Aquaro, G.D. Design and simulation of a dual-tuned ^{1}H/^{23}Na birdcage coil for MRS studies in human calf. *Appl. Magn. Reson.* **2015**, *46*, 1221–1238. [CrossRef]

26. Choi, C.-H.; Hutchison, J.M.; Lurie, D.J. Design and construction of an actively frequency-switchable RF coil for field-dependent Magnetisation Transfer Contrast MRI with fast field-cycling. *J. Magn. Reson.* **2010**, *207*, 134–139. [CrossRef] [PubMed]

27. Choi, C.-H.; Hong, S.-M.; Ha, Y.; Shah, N.J. Design and construction of a novel ^{1}H/^{19}F double-tuned coil system using PIN-diode switches at 9.4 T. *J. Magn. Reson.* **2017**, *279*, 11–15. [CrossRef]

28. Shen, G.X.; Boada, F.E.; Thulborn, K.R. Dual-frequency, dual-quadrature, birdcage RF coil design with identical B_1 pattern for sodium and proton imaging of the human brain at 1.5 T. *Magn. Reson. Med.* **1997**, *38*, 717–725. [CrossRef]

29. Shen, G.X.; Wu, J.; Boada, F.E.; Thulborn, K.R. Experimentally verified, theoretical design of dual-tuned, low-pass birdcage radiofrequency resonators for magnetic resonance imaging and magnetic resonance spectroscopy of human brain at 3.0 Tesla. *Magn. Reson. Med. Off. J. Int. Soc. Magn. Reson. Med.* **1999**, *41*, 268–275. [CrossRef]

30. Rath, A.R. Design and performance of a double-tuned bird-cage coil. *J. Magn. Reson.* **1990**, *86*, 488–495. [CrossRef]

31. Murphyboesch, J.; Srinivasan, R.; Carvajal, L.; Brown, T.R. Two configurations of the four-ring birdcage coil for ^{1}H imaging and ^{1}H-decoupled ^{31}P spectroscopy of the human head. *J. Magn. Reson. Ser. B* **1994**, *103*, 103–114. [CrossRef] [PubMed]

32. Tomanek, B.; Volotovskyy, V.; Gruwel, M.L.; Mckenzie, E.; King, S.B. Double-frequency birdcage volume coils for 4.7 T and 7T. *Concepts Magn. Reson. Part B Magn. Reson. Eng. Educ. J.* **2005**, *26*, 16–22. [CrossRef]

33. Lim, H.; Thind, K.; Martinez-Santiesteban, F.M.; Scholl, T.J. Construction and evaluation of a switch-tuned ^{13}C-^{1}H birdcage radiofrequency coil for imaging the metabolism of hyperpolarized ^{13}C-enriched compounds. *J. Magn. Reson. Imaging* **2014**, *40*, 1082–1090. [CrossRef] [PubMed]

34. Isaac, G.; Schnall, M.D.; Lenkinski, R.E.; Vogele, K. A design for a double-tuned birdcage coil for use in an integrated MRI/MRS examination. *J. Magn. Reson. (1969)* **1990**, *89*, 41–50. [CrossRef]

35. Lykowsky, G.; Carinci, F.; Düring, M.; Weber, D.; Jakob, P.M.; Haddad, D. Optimization and comparison of two practical dual-tuned birdcage configurations for quantitative assessment of articular cartilage with sodium magnetic resonance imaging. *Quant. Imaging Med. Surg.* **2015**, *5*, 799. [PubMed]

36. Yee, K. Numerical solution of initial boundary value problems involving Maxwell's equations in isotropic media. *IEEE Trans. Antennas Propag.* **1966**, *14*, 302–307.

37. Sim4Life, ZMT Zurich MedTech AG. Available online: https://zmt.swiss/sim4life/ (accessed on 28 September 2023).

38. Kumar, S.; Chung, H.-J.; Jeong, Y.-J.; Lee, H.-K.; Oh, C.-H. Design and Implementation of Split-Leg Type Elliptical Whole-Body Birdcage RF Coil at 1.5 T MRI. *Appl. Sci.* **2021**, *16*, 7448. [CrossRef]

39. Chin, C.L.; Collins, C.M.; Li, S.; Dardzinski, B.J.; Smith, M.B. BirdcageBuilder: Design of specified-geometry birdcage coils with desired current pattern and resonant frequency. *Concepts Magn. Reson.* **2002**, *15*, 156–163. [CrossRef]

40. Christ, A.; Kainz, W.; Hahn, E.G.; Honegger, K.; Zefferer, M.; Neufeld, E.; Rascher, W.; Janka, R.; Bautz, W.; Chen, J. The Virtual Family—Development of surface-based anatomical models of two adults and two children for dosimetric simulations. *Phys. Med. Biol.* **2009**, *55*, N23. [CrossRef]

41. Peterson, D.M.; Beck, B.L.; Duensing, G.R.; Fitzsimmons, J.R. Common mode signal rejection methods for MRI: Reduction of cable shield currents for high static magnetic field systems. *Concepts Magn. Reson. Part B Magn. Reason. Eng.* **2003**, *19*, 1–8. [CrossRef]

42. Oh, C.-H.; Jeong, Y.-J.; Kumar, S. Construction Method and Signal Acquisition Method for Dual-Mode Radio Frequency Coil to Acquire Magnetic Resonance Signals from Two Kinds of Nuclei. Korea Patent. Pending.

43. Yarnykh, V.L. Actual flip-angle imaging in the pulsed steady state: A method for rapid three-dimensional mapping of the transmitted radiofrequency field. *Magn. Reson. Med. Off. J. Int. Soc. Magn. Reson. Med.* **2007**, *57*, 192–200. [CrossRef]

44. Kumar, S.; Yoon, J.-S.; Kim, J.-M.; Lee, C.; Oh, C.-H. Whole-brain imaging with receive-only multichannel top-hat dipole antenna RF coil at 7 T MRI. *J. Korean Phys. Soc.* **2022**, *80*, 920–927. [CrossRef]

45. Cunningham, C.H.; Pauly, J.M.; Nayak, K.S. Saturated double-angle method for rapid B_{1+} mapping. *Magn. Reson. Med. Off. J. Int. Soc. Magn. Reson. Med.* **2006**, *55*, 1326–1333. [CrossRef]

46. ISMRM Best Practices for Safety Testing of Experimental RF Hardware. Available online: https://www.ismrm.org/working-groups/best-practices-for-safety-testing-of-experimental-rf-hardware/ (accessed on 28 September 2023).

47. Steensma, B.R.; Sadeghi-Tarakameh, A.; Meliadò, E.F.; van den Berg, C.A.; Klomp, D.W.; Luijten, P.R.; Metzger, G.J.; Eryaman, Y.; Raaijmakers, A.J. Tier-based formalism for safety assessment of custom-built radio-frequency transmit coils. *NMR Biomed.* **2023**, *36*, e4874. [CrossRef]

48. Jackson, E.; Bronskill, M.; Drost, D.; Och, J.; Pooley, R.; Sobol, W.; Clarke, G. *AAPM Report MR TG-1: Acceptance Testing and Quality Assurance Procedures for Magnetic Resonance Imaging Facilities*; American Association of Physicists in Medicine: Alexandria, VA, USA, 2010.

49. *IEC 60601-2-33:2010*; Medical Electrical Equipment—Part 2–33: Particular Requirements for the Basic Safety and Essential Performance of Magnetic Resonance Equipment for Medical Diagnosis, 3rd ed. IEC: Geneva, Switzerland, 2015.

50. Yu, Z.; Madelin, G.; Sodickson, D.K.; Cloos, M.A. Simultaneous proton magnetic resonance fingerprinting and sodium MRI. *Magn. Reson. Med.* **2020**, *83*, 2232–2242. [CrossRef]

51. Madelin, G.; Lee, J.-S.; Regatte, R.R.; Jerschow, A. Sodium MRI: Methods and applications. *Prog. Nucl. Magn. Reson. Spectrosc.* **2014**, *79*, 14–47. [CrossRef] [PubMed]